

Journal of Biomedical Optics

BiomedicalOptics.SPIEDigitalLibrary.org

Two-photon spectral fluorescence lifetime and second-harmonic generation imaging of the porcine cornea with a 12-femtosecond laser microscope

Ana Batista
Hans Georg Breunig
Aisada Uchugonova
António Miguel Morgado
Karsten König

Two-photon spectral fluorescence lifetime and second-harmonic generation imaging of the porcine cornea with a 12-femtosecond laser microscope

Ana Batista,^{a,b,*} Hans Georg Breunig,^{a,c} Aisada Uchugonova,^a António Miguel Morgado,^{b,d} and Karsten König^{a,c}

^aSaarland University, Faculty of Physics and Mechatronics, Department of Biophotonics and Laser Technology, Campus A5.1, Saarbrücken 66123, Germany

^bUniversity of Coimbra, Faculty of Medicine, Institute for Biomedical Imaging and Life Sciences, Azinhaga Santa Comba—Celas, Coimbra 3000-548, Portugal

^cJenLab GmbH, Schillerstr. 1, Jena 07745, Germany

^dUniversity of Coimbra, Faculty of Sciences and Technology, Department of Physics, Rua Larga, Coimbra 3004-516, Portugal

Abstract. Five dimensional microscopy with a 12-fs laser scanning microscope based on spectrally resolved two-photon autofluorescence lifetime and second-harmonic generation (SHG) imaging was used to characterize all layers of the porcine cornea. This setup allowed the simultaneous excitation of both metabolic cofactors, NAD(P)H and flavins, and their discrimination based on their spectral emission properties and fluorescence decay characteristics. Furthermore, the architecture of the stromal collagen fibrils was assessed by SHG imaging in both forward and backward directions. Information on the metabolic state and the tissue architecture of the porcine cornea were obtained with subcellular resolution, and high temporal and spectral resolutions. © 2016 Society of Photo-Optical Instrumentation Engineers (SPIE) [DOI: 10.1117/1.JBO.21.3.036002]

Keywords: cornea imaging; two-photon autofluorescence; fluorescence lifetime imaging; second-harmonic generation; metabolic imaging; NAD(P)H; flavins.

Paper 150720R received Oct. 27, 2015; accepted for publication Feb. 12, 2016; published online Mar. 8, 2016.

1 Introduction

Multiphoton microscopy (MPM) has surfaced in the past years as an important imaging method in the biological field.¹ The high penetration depth combined with the pinhole-free optical sectioning capability of this imaging modality allows three-dimensional (3-D) imaging of biological tissues with subcellular resolution. Therefore, using MPM, the entire thickness of the cornea can be imaged with information on both the morphology and cell metabolism.² This information could be used in the clinical practice to improve the diagnosis of corneal pathologies.

The cornea, the outermost transparent structure of the eye, is responsible for two-thirds of the eye's refractive power.^{3,4} Anatomically, the porcine cornea is composed of four layers: the epithelium, stroma, Descemet's membrane, and endothelium.⁵ The epithelium is composed of sublayers of superficial, wing, and basal cells.^{3,4} Basal cells are the only cells with mitotic activity and differentiate progressively into wing and superficial cells.³ The stroma, mainly composed of collagen fibrils, represents ~90% of the total corneal thickness.^{3,4} Between the stroma and the endothelium lies the Descemet's membrane, which is mainly composed of collagen and glycoproteins such as laminin and fibronectin.⁴ The endothelium is a single layer of polyhedral cells with regular shape and dimensions.^{3,4} In contrast to the human cornea, the porcine cornea does not have Bowman's layer.⁵

The cornea is most commonly imaged in the clinical practice using corneal confocal laser scanning microscopy (CLSM) or optical coherence tomography (OCT). These imaging modalities

provide insightful structural information of the cornea. However, with MPM both the tissue structure and metabolic state of its cells are addressed.² OCT is based on the detection of backscattered photons and provides a cross-sectional view of the cornea, providing information on the corneal thickness, as well as discrimination of different corneal layers.⁶ In the past years, some functional extensions of OCT have also emerged.⁷ However, the assessment of cell metabolism is still not possible. Furthermore, OCT resolution is limited.⁷ In CLSM, pinholes are used to block the out-of-focus light, thus conferring it subcellular resolution. CLSM gives information on the corneal cell morphology and nerve density.⁸ However, due to its inability to image the collagen fibrils present in the stroma, CLSM disregards the major component of the cornea. Further advantages of MPM over CLSM in the analysis of different ocular surface pathologies have been described by Steven et al.⁹

The metabolic state of corneal cells can be assessed through fluorescence lifetime imaging microscopy (FLIM), based on the intrinsic fluorescence of the metabolic cofactors NAD(P)H (nicotinamide adenine dinucleotide/nicotinamide adenine dinucleotide phosphate) and flavins (flavin mononucleotide/flavin adenine dinucleotide). The assessment of the metabolic cell state can be based on both the autofluorescence intensity and the lifetime. The autofluorescence intensity of NAD(P)H has been already successfully used to determine the metabolic state of the rabbit's cornea after incubation with inhibitors of the mitochondrial chain¹⁰ and as a contrast mechanism to discriminate all layers of the rabbit's cornea *in vivo*.¹¹ However, using the autofluorescence lifetime has several advantages. Unlike the

*Address all correspondence to: Ana Batista, E-mail: amgbatista@fmed.uc.pt

autofluorescence intensity, the lifetime is specific for each fluorophore and nearly independent of the molecular concentration.² Another important feature is its sensitivity to the fluorophore microenvironment, which allows to discriminate free from protein-bound fluorophores.² Since the alternation between free and protein-bound states NAD(P)H and flavins occurs during the energy production mechanisms of the cells,¹² the quantification of these components through FLIM presents itself as a robust measure of the metabolic state.

FLIM was introduced to life sciences (imaging of live cells and animals) in 1989,¹³ and it was first applied on humans about one decade later to image both dental caries¹⁴ and the skin *in vivo*.¹⁵ The first results obtained with a two-photon excitation FLIM certified medical device were published in 2002 by König et al.¹⁶ In the ophthalmologic field, pioneering work has been conducted by Schweitzer et al.¹⁷, using a CLSM modified to acquire one-photon excitation FLIM images of the human retina *in vivo*. This system has already been shown to be efficient for the diagnosis of ocular pathologies such as age-related macular degeneration¹⁸ or diabetic retinopathy.¹⁹

The fibrillary structures, composed mainly of collagen type I, present in the corneal stroma can be imaged by second-harmonic generation (SHG) imaging. This imaging modality was first applied to image biological tissues by Fine and Hansen in 1971.²⁰ Its capability to image structures with noncentrosymmetric organization like collagen,²¹ makes SHG ideal for the assessment of the stromal architecture. SHG generated photons propagate mainly in the forward direction. However, in scattering media, such as biological tissues, multiple scattering gives rise to forward and backward direction SHG signals.²¹ SHG imaging was already successfully used to assess morphological alterations due to keratoconus²² and corneal collagen crosslinking.²³

Here, we report on the use of a unique five-dimensional (5-D)-MPM microscope with high spatial, temporal, and spectral resolution to image and characterize all layers of the porcine cornea. The metabolic state of the corneal cells was assessed based on the autofluorescence lifetime of both metabolic

cofactors, NAD(P)H and flavins. A characterization of basal, wing, and superficial cell's individual metabolic states was addressed. Furthermore, the structural organization of collagen fibrils in the corneal stroma was analyzed in both forward and backward directions. The autofluorescence lifetime of the Descemet's membrane was also described.

2 Material and Methods

2.1 Porcine Corneal Samples

Freshly enucleated porcine eyes were obtained 1 h after animal sacrifice from a local slaughterhouse and kept in phosphate buffered saline at room temperature. A corneal trephine blade (Katena Products Inc., New Jersey) with a 9.0-mm diameter was used to cut the central part of the cornea which was then placed in a glass bottom petri dish for MPM imaging. In order to minimize morphological and physiological changes, the isolated corneal tissue was situated in a physiological medium (#A14291DJ, Life Technologies, California) especially designed for live cell imaging and the entire image acquisition time was kept below 4 h following sample dissection. For imaging of the Descemet's membrane and endothelial layers, the sample was flipped.

A total of 17 corneal samples were used. Up to two different areas were acquired from each sample.

2.2 Imaging Instrumentation

Measurements were performed using a near-infrared 12-fs laser scanning microscope (JenLab GmbH, Jena, Germany), consisting of an inverted microscope (Axio Observer D1; Carl Zeiss, Jena, Germany) with a galvanometric scanner unit, a beam expander, a dichroic mirror, and a 40× NA 1.3 oil immersion objective with a working distance of 210 μm (EC Plan-Neofluar 40×, NA 1.3; Carl Zeiss, Jena, Germany) for focusing the laser light and signal collection [Fig. 1(a)]. Sample excitation was achieved using a mode-locked titanium-sapphire laser

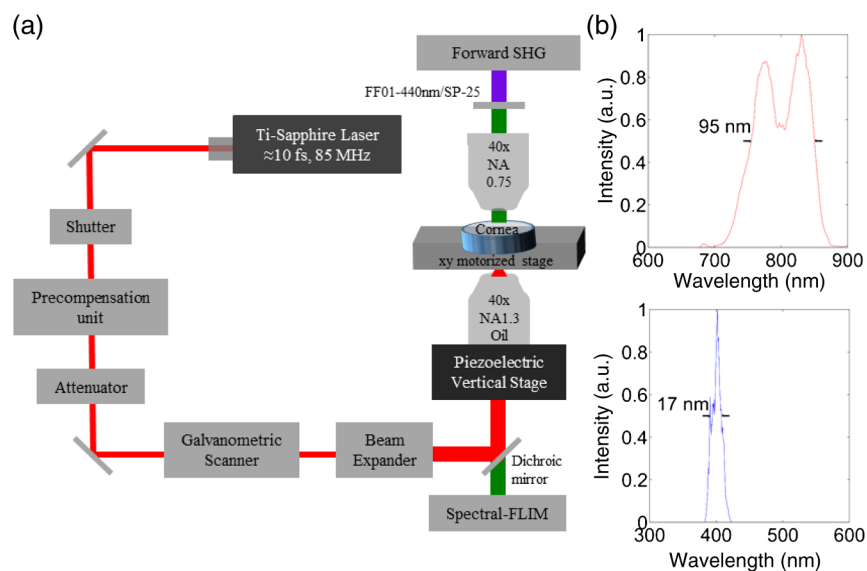


Fig. 1 (a) 5-D multiphoton microscope with submicron resolution, 170 ps temporal resolution, and 12.5 nm spectral resolution for two-photon excitation autofluorescence lifetime and SHG imaging of the porcine cornea. The *in situ* pulse width was 12 fs. (b) Laser (top) and SHG (bottom) spectra. The full width at half maximum of each spectrum are as indicated.

(Integral Pro 400; Femtolasers Produktions GmbH, Vienna, Austria) generating broadband pulses at a frequency of 85 MHz. The laser spectrum was centered at ~ 800 nm with an M-shaped spectral profile and a bandwidth of about 95 nm [Fig. 1(b)]. The group velocity dispersion was precompensated using chirped mirrors to obtain a pulse width of 12 fs behind the objective, which was confirmed by autocorrelation measurements.²⁴

Autofluorescence signals were detected using a 16 channel PMT detector (16PML-PMT, Becker & Hickl GmbH) associated with a time-correlated single photon counting (TCSPC) SPC-150 module (Becker & Hickl GmbH, Berlin, Germany) for TCSPC. The instrument response function (IRF), with a full width at half maximum (FWHM) of 169.5 ps, was obtained by measuring the apparent SHG decay profile from crystallized urea.

The number of photons detected in each pixel was used to create a grey-scale intensity-based image, while the fluorescence lifetime was used to create pseudo-color FLIM images.

SHG signals were simultaneously detected in forward and backward directions using a single channel PMT detector (H7732; Hamamatsu Photonics, Hamamatsu, Japan) and the 16 channel PMT detector, respectively. Images detected in the forward direction were acquired during 7.4-s for images with 512×512 pixels. A 440-nm short-pass filter (FF01-440/SP-25, Semrock, Inc., New York) was used to block the autofluorescence signals in this case.

2.3 Image Analysis

The fluorescence lifetime images were analyzed using the commercial software SPCImage version 4.9.7 (Becker & Hickl GmbH, Berlin, Germany). Fluorescence lifetimes were obtained after deconvolution of the measured decay with the IRF by application of a two-exponential decay fit of the form $F(t) = a_1 e^{-t/\tau_1} + a_2 e^{-t/\tau_2}$, where $F(t)$ is the fluorescence intensity at time t , and a_1 and a_2 ($a_1 + a_2 = 1$) are the fractional contributions of the fluorescence lifetimes τ_1 and τ_2 , respectively. The mean autofluorescence lifetime was computed as $\tau_m = a_1 \tau_1 + a_2 \tau_2$.

The 16 channel PMT detector used for signal detection had a spectral range of detection between 400 and 600 nm (each channel with a spectral width of 12.5 nm). For the individual analysis of NAD(P)H, flavins and collagen autofluorescence, the spectra of solutions of nicotinamide adenine dinucleotide, and flavin adenine dinucleotide (FAD) in Tris hydrochloride solution, and lyophilized collagen type I were acquired using the 5-D 12-fs laser microscope.²⁵ Based on the channels in which the individual spectra were detected,²⁵ the following spectral ranges were selected:

Range I (NAD(P)H autofluorescence)—Channels 3 to 8 (425 to 500 nm);

Range II (flavins autofluorescence)—Channels 9 to 14 (500 to 575 nm);

Range III (autofluorescence)—Channels 3 to 14 (425 to 575 nm).

The selection of the spectral intervals used for SHG analysis was based on the SHG spectrum from crystallized urea [Fig. 1(b)]. The obtained SHG spectrum was narrower (17 nm) than the SHG spectrum expected for transformed limited pulses.^{26,27} This is most likely a result of a residual chirp of

the pulse. Nevertheless, the SHG spectrum is broader than each individual channel of the PMT, and a strong SHG signal can be detected in the first two channels.²⁵ The following spectral interval was chosen for SHG analysis:

Range IV (SHG)—Channels 1 to 2 (400 to 425 nm).

To analyze the changes in collagen fibril architecture with depth, xy and xz projections, as well as 3-D representations of the SHG signals, were created by acquiring sequential SHG images ($2 \mu\text{m}$ apart) in backward and forward directions. The 3-D volumes were then rendered using the Visualization Toolkit (VTK) within MATLAB (The MathWorks, Inc.).²⁸

3 Results

3.1 Optical Window for Safe 5-D Multiphoton Microscopy

FLIM image acquisition was performed using mean laser powers between 10 and 15 mW, depending on the depth. Typical dwell time of 0.11 ms/pixel, corresponding to the acquisition time of 7.4 s/frame for images with 256×256 pixels were used. Images were averaged over 9 to 13 frames. With these acquisition parameters, higher autofluorescence intensities (higher photon counts) were observed in the NAD(P)H range compared to the flavins range [Fig. 2(a)]. The photon counts are the sum of all photons counted in all pixels.

Laser induced damage using these acquisition parameters was assessed by imaging the corneal epithelium 20 consecutive times using a laser power of 15 mW and beam dwell time of 0.11 ms/pixel. Based on single photon counting detection, a slight decrease in the normalized autofluorescence intensity was observed within the first 10 images (from 1.00 to 0.96), stabilizing after this value [Fig. 2(b)]. No visible lesions or morphological changes in cells were observed between the different images acquired [Fig. 2(c)].

3.2 Optical Sectioning

Using the 5-D 12-fs laser microscope, images of the porcine cornea, with a $2\text{-}\mu\text{m}$ depth interval, were acquired for all corneal layers. In Fig. 3, an xz cross-section of the porcine cornea autofluorescence intensity and SHG signals is shown [Fig. 3(a)]. For a better visualization of each layer morphology, autofluorescence intensity and SHG images at multiple depths are also shown [Fig. 3(b)].

Based on the autofluorescence intensity of both metabolic cofactors and SHG signals, we were able to visualize and discriminate between all corneal layers, as well as the interfaces between them. Furthermore, in the corneal epithelium, discrimination between different cell types was achieved. Superficial cells ($d = 0 \mu\text{m}$ and $d = 22 \mu\text{m}$), wing cells ($d = 34 \mu\text{m}$ and $d = 58 \mu\text{m}$), and basal cells ($d = 78 \mu\text{m}$) are shown in Fig. 3.

A high density of mitochondria in the basal cells, located preferentially around the nuclei, was visible [Fig. 3(b)]. Toward the surface, the number of mitochondria reduces and they became more disperse. The upmost superficial cells ($d = 0 \mu\text{m}$) have a reduced number of mitochondria [Fig. 3(b)].

In the porcine cornea, the stroma can be found immediately behind the epithelium.⁵ The interface between these layers starts at a corneal depth of $88 \mu\text{m}$ [Fig. 3(b)]. Here, both autofluorescence signals from the metabolic active basal cells and SHG signals from the collagen fibrils in the stroma are visible.

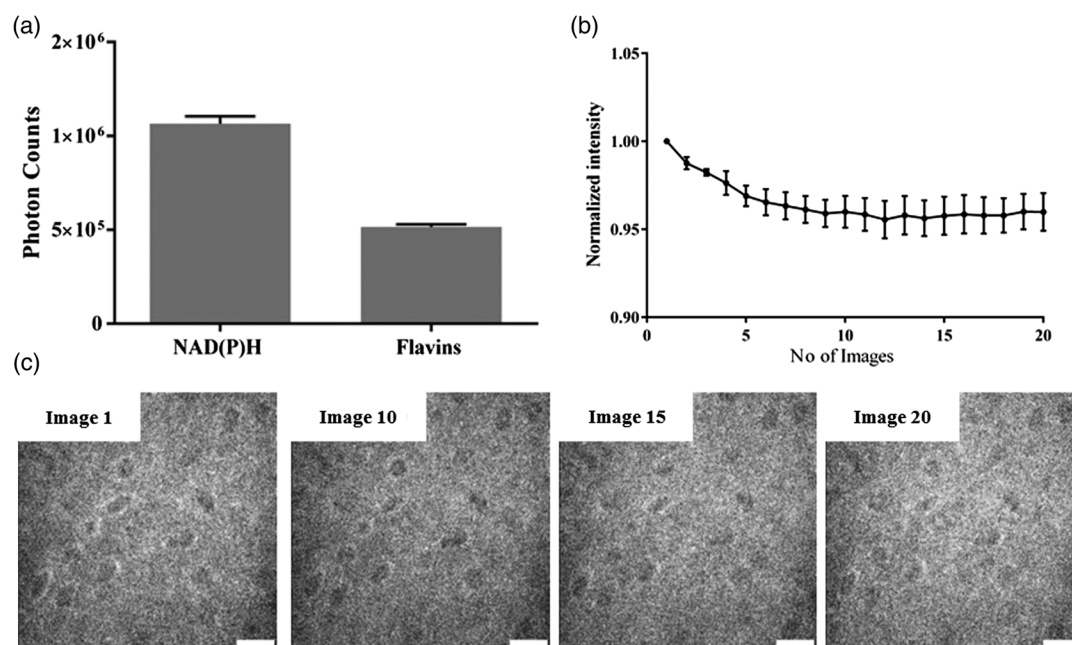


Fig. 2 (a) NAD(P)H and flavins autofluorescence intensity detected with the 5-D 12-fs laser scanning microscope. Alterations caused by 20 times consecutive imaging to (b) the total autofluorescence intensity and (c) to the corneal cell anatomy. For the analysis of laser-induced damage by consecutive image acquisition the autofluorescence intensity of both metabolic co-factors was taken into account. Scale bar = 20 μm .

It can also be perceived that the corneal epithelial thickness is not constant along the corneal surface (Fig. 3).

The SHG signals originating from the collagen fibrils in the corneal stroma, collected in the backward direction, are shown at corneal depths of 94 and 128 μm (Fig. 3). The individual collagen fibrils were not distinguishable in the images. Instead, diffuse and speckle-like signals were visible. Although present, the autofluorescence signal of this corneal layer is negligible compared to the SHG signal.

In the Descemet's membrane, autofluorescence signals were observed [Fig. 3(b)]. Although composed mainly of collagen, no SHG signals were detected.

The well-organized endothelial cells were also distinguished based on their autofluorescence intensity [Fig. 3(b)]. Regularly shaped cells with widths of approximately $(24.3 \pm 2.2) \mu\text{m}$ were observed. Based on the number of the cells observed in the field of view, an endothelial cell density of $(2350 \pm 146) \text{ cells/mm}^2$ was estimated for the porcine cornea samples.

Thicknesses between 70 and 80 μm ($\pm 2 \mu\text{m}$) were measured for the porcine cornea epithelium. The corneal endothelium was between 6 and 8 μm ($\pm 2 \mu\text{m}$) thick, while the Descemet's membrane was 6 to 10 μm ($\pm 2 \mu\text{m}$) thick.

3.3 Spectral Fluorescence Lifetime Imaging Microscopy of the Cornea

For each layer of the cornea, fluorescence lifetime images were acquired with spectral separation of the endogenous fluorophore signals. In Fig. 4, the autofluorescence intensity image and corresponding FLIM images of the porcine cornea epithelial wing cells, stroma, Descemet's membrane, and endothelium are shown. In the case of the epithelial and endothelial cells, the FLIM images are pseudo-color coded for NAD(P)H mean

autofluorescence lifetime (range I), while for the stroma and Descemet's membrane the mean autofluorescence lifetime (range III) is used. The range of the autofluorescence lifetime values are as indicated in the color bar.

The fluorescence lifetimes observed in each corneal layer are shown in Table 1. In the porcine cornea epithelium and endothelium the autofluorescence lifetimes NAD(P)H (range I) and flavins (range II) were analyzed separately. In the stroma and Descemet's membrane no spectral division was performed within the autofluorescence signals (range III).

In the corneal stroma, the autofluorescence signals arise from both collagen and keratocytes. In Fig. 4, white arrows point out keratocytes with dendritic/stellate shapes.²⁹ With this experimental setup there is a high overlap between autofluorescence of collagen and the metabolic cofactors, in particular NAD(P)H.²⁵ Therefore, a spectral separation of keratocytes and collagen autofluorescence is challenging. FLIM analysis of single keratocytes was performed by selecting regions of interest. Keratocytes had a mean lifetime of $0.87 \text{ ns} \pm 0.04 \text{ ns}$ and a free to protein-bound ratio of 2.48 ± 0.46 . A mean autofluorescence lifetime of $0.64 \text{ ns} \pm 0.08 \text{ ns}$ was observed in the regions of interest where only collagen autofluorescence was present.

Slight differences were observed between the epithelial and endothelial layers in the NAD(P)H and flavins autofluorescence lifetimes and relative contributions (Table 1), which may indicate differences in their metabolic activity. In the endothelial layer, the NAD(P)H free to protein-bound ratio was lower than in the epithelium. For flavins, the opposite was observed.

The metabolic state of the different cells composing the epithelium was also analyzed. The autofluorescence intensity images and the corresponding FLIM images of the corneal epithelium at multiple depths are shown in Fig. 5(a). For a better visualization of NAD(P)H and flavins lifetime variations with

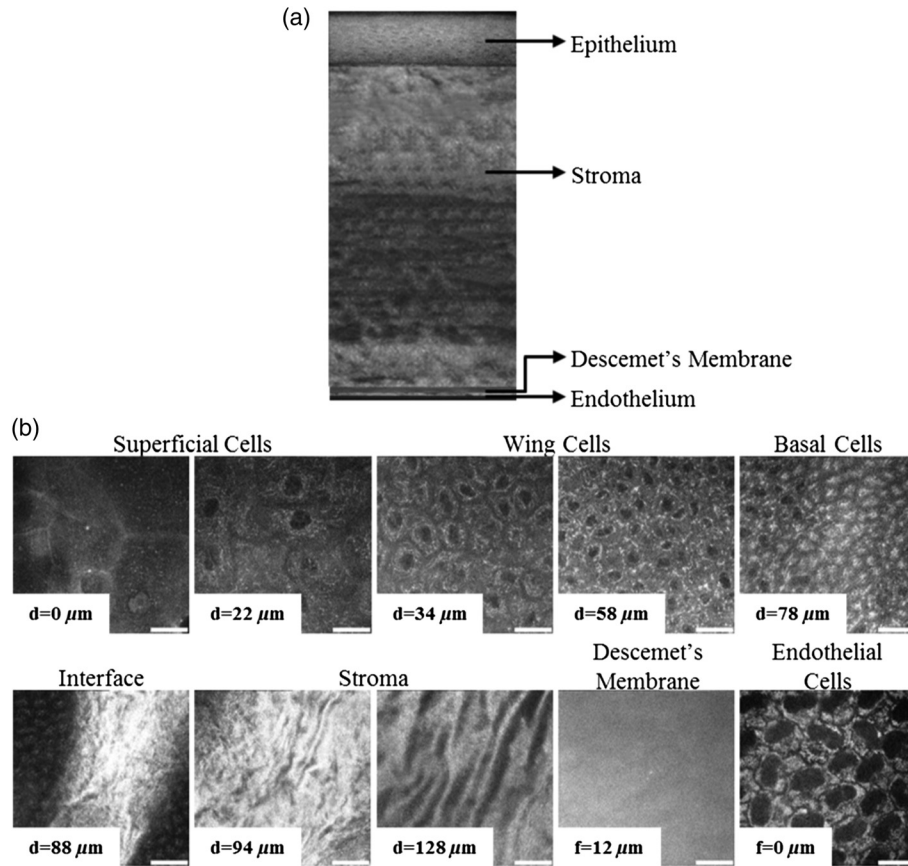


Fig. 3 (a) x-z cross-section of the porcine cornea. (b) Autofluorescence intensity images of the porcine corneal epithelial superficial cells (0 and 22 μm), wing cells (34 and 58 μm), basal cells (78 μm), SHG images of corneal stroma (94 and 128 μm) and autofluorescence intensity images of Descemet's membrane (12 μm), and endothelial cells (0 μm) after flipping the samples. At the interface between the epithelium and stroma (88 μm) both autofluorescence intensity and second harmonic generation signals are detected. The signal intensity in each pixel represents the number of detected photons. The corneal tissue depth is indicated in each image. The distance f is measured relative to the corneal endothelium. Scale bar = 20 μm .

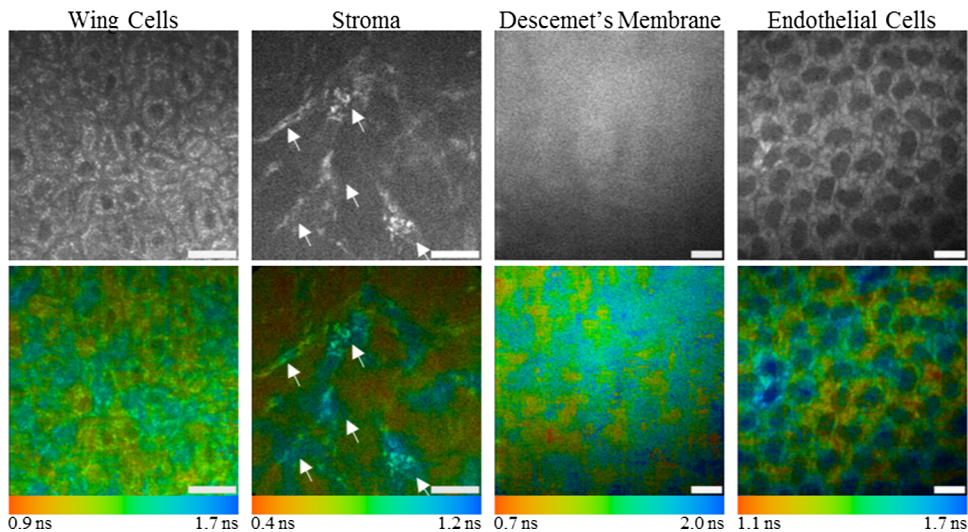


Fig. 4 Autofluorescence intensity (top row) and corresponding FLIM images (bottom row) of the cornea. In the autofluorescence intensity images, the signal intensity represents the number of photons detected in each pixel. FLIM images are pseudo-color coded for NAD(P)H mean autofluorescence lifetime (range I). The stroma and Descemet's membrane FLIM images are pseudo-color coded for the mean autofluorescence lifetime in spectral range III. Autofluorescence lifetime ranges are as indicated in the color bars. Keratocytes in dendritic/stellate shape in the corneal stroma are indicated by the white arrows. Scale bar = 20 μm .

Table 1 Porcine cornea layer's autofluorescence lifetimes, their relative contribution, and their free to protein-bound ratio. Values are represented as mean \pm standard deviation.

Corneal layer	Epithelium (averaged)				Endothelium	
	NAD(P)H	Flavins	Stroma	Descemet's membrane	NAD(P)H	Flavins
τ_1 (ns)	0.49 ± 0.07	0.55 ± 0.07	0.26 ± 0.06	0.35 ± 0.05	0.53 ± 0.07	0.50 ± 0.04
τ_2 (ns)	2.42 ± 0.16	2.47 ± 0.89	2.36 ± 0.16	2.61 ± 0.06	2.43 ± 0.17	2.14 ± 0.27
τ_m (ns)	1.34 ± 0.21	1.17 ± 0.18	0.82 ± 0.22	1.35 ± 0.17	1.37 ± 0.10	1.15 ± 0.12
a_1 (%)	56.0 ± 6.9	65.0 ± 8.3	73.3 ± 7.4	55.7 ± 5.9	55.9 ± 2.7	60.1 ± 6.0
a_2 (%)	44.0 ± 6.9	35.0 ± 8.3	26.7 ± 7.4	44.3 ± 5.9	44.1 ± 2.7	39.9 ± 6.0
free/(protein – bound)	1.33 ± 0.36	0.56 ± 0.19	—	—	1.27 ± 0.13	0.68 ± 0.17

depth, their mean autofluorescence lifetimes are represented as a function of depth in Fig. 5(b).

A decrease in the mean autofluorescence lifetimes with the corneal depth was observed for both NAD(P)H and flavins (Fig. 5). Furthermore, for NAD(P)H, the free to protein-bound ratio increases with depth, while that for flavins decreases (Table 2). This suggests changes in metabolic activity with depth. A decrease in the photon counts detected in the NAD(P)H and flavins range is also observed with depth. In Table 2, the autofluorescence intensities of both metabolic co-factors normalized for the NAD(P)H autofluorescence intensity are also shown.

3.4 Corneal Stroma Second-Harmonic Generation

In the corneal stroma, two distinct signals can be detected: autofluorescence (Fig. 4) and SHG (Fig. 6). Although both signals are present, the autofluorescence signals are usually weaker than the SHG signals and can only be detected after spectral separation of the detected signals. In the porcine corneal stroma the autofluorescence signal intensity (range III) detected was 1/3 ($\pm 1/7$) that of the SHG signal intensity (range IV).

Significantly different corneal stroma SHG images were obtained with backward and forward detection configurations. As previously described, backward SHG images of the stroma present a homogenous signal intensity [Fig. 6(a)] and information about the collagen fibrils orientation was not directly visible. On the other hand, in forward SHG images of the same area [Fig. 6(b)] the architecture of the collagen fibrils was visible.

For both detection configurations, xz and yz projections of the SHG signals were created and are shown in Figs. 6(a) and 6(b). Furthermore, 3-D representations of the SHG signals of approximately $153 \times 153 \times 40 \mu\text{m}^3$ of the same data are shown in Figs. 6(c) and 6(d).

4 Discussion

In this study, the porcine cornea was characterized based on spectrally and spatially resolved FLIM and SHG. The simultaneous acquisition of both metabolic cofactors autofluorescence lifetimes provides a robust measure of the corneal cell's metabolism. Furthermore, the simultaneous SHG and autofluorescence imaging from the corneal stroma provides information not only on the collagen fibrils structural but also on keratocytes metabolic activity.

Safety parameters are an essential issue to consider when imaging biological samples. Therefore, we tested the acquisition parameters (laser power and beam dwell time per pixel) to ensure enough photons' detection without damage to the sample. A sufficiently high number of detected photons (intensity) is important not only to acquire high contrast images, where single cells can be visualized, but also to ensure a precise analysis of the fluorescence lifetimes.³⁰

FLIM acquisition with the 16-channel PMT detector required high laser powers, long pixel dwell times, and image averaging. Resorting to a single channel PMT detector, images can be acquired with a pixel dwell time of 0.03 ms/pixel without further averaging. This shows that the 16 channel PMT detector is better suitable for imaging exogenous fluorophores which are present in higher concentrations. However, despite the imaging parameters selected, no tissue damage was observed (Fig. 2). After 20 consecutive images, a slight decrease in the autofluorescence intensity was observed due to photobleaching [Fig. 2(b)] without changes to the cell morphology [Fig. 2(c)]. High laser powers have also been described for *in vivo* imaging of the skin.³¹

Using the selected acquisition parameters, higher autofluorescence intensities were observed for NAD(P)H than for flavins [Fig. 2(a)]. Considering the spectral properties of the excitation laser source (central wavelength at 800 nm) and the two-photon excitation action cross sections of NAD(P)H and flavins,³² we conclude that the main factor limiting the flavins autofluorescence intensity is its relatively low concentration in the cornea.^{33,34}

FLIM combined with SHG enables imaging and discrimination of all corneal layers (Fig. 3). The feasibility of these imaging modalities to discriminate between different layers of the porcine cornea has already been reported.^{35–38} The cornea endothelium and epithelium emit endogenous fluorescence from the metabolic cofactors NAD(P)H and flavins. NAD(P)H is present both in the cell's cytoplasm and mitochondria, while flavins are present exclusively in the energy production organelles.³⁹ Therefore, the cells exhibit autofluorescence mainly in the cytoplasm and mitochondria while the nucleus and membrane lack autofluorescence signals. This allows single cell visualization.

In the corneal epithelium superficial, wing, and basal cells were observed [Fig. 3(b)]. The discrimination between cell types was possible based on the cells morphology. The loss of organelles, including mitochondria, characteristic of the progressive

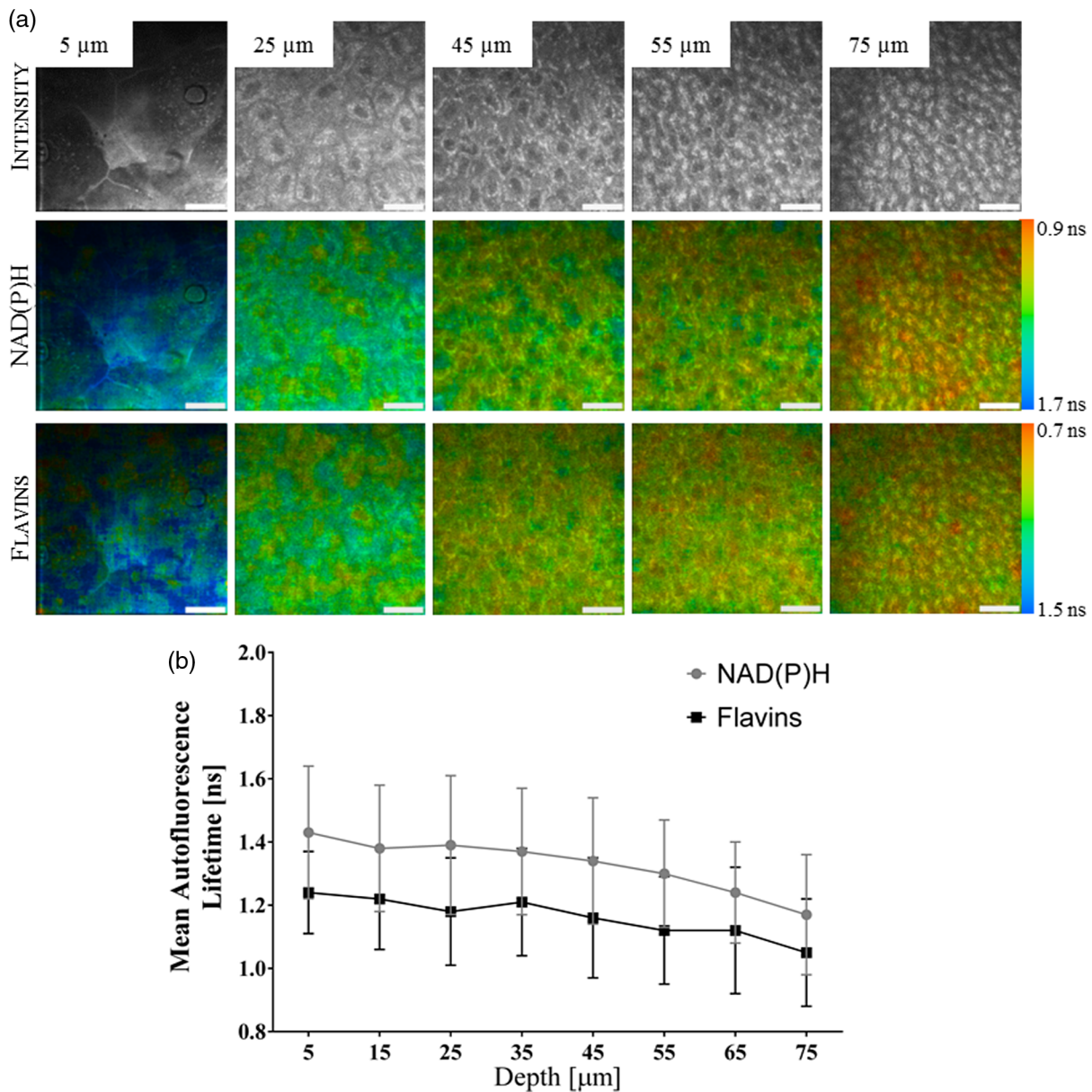


Fig. 5 Porcine cornea epithelium (a) autofluorescence intensity and corresponding FLIM images pseudo-color coded for NAD(P)H and flavins mean autofluorescence lifetime at multiple depths. Autofluorescence lifetime value ranges are as indicated by the color bars. (b) Depth-resolved mean autofluorescence lifetimes in the NAD(P)H and flavins ranges (the bars indicate standard deviation). Scale bar = 20 μm .

differentiation of basal cells into wing and superficial cell,³ was observed due to the feasibility of FLIM to resolve single mitochondria [Fig. 3(b)].

The assessment of endothelial cells morphological characteristics, such as cell widths and density [Fig. 3(b)] provides insightful information on the state of this layer, since the proper function of the endothelium is highly correlated with its cell density (endothelial cells do not regenerate).³ The endothelial cell widths and cell densities measured are consistent with those reported for porcine cornea endothelial cells.⁴⁰

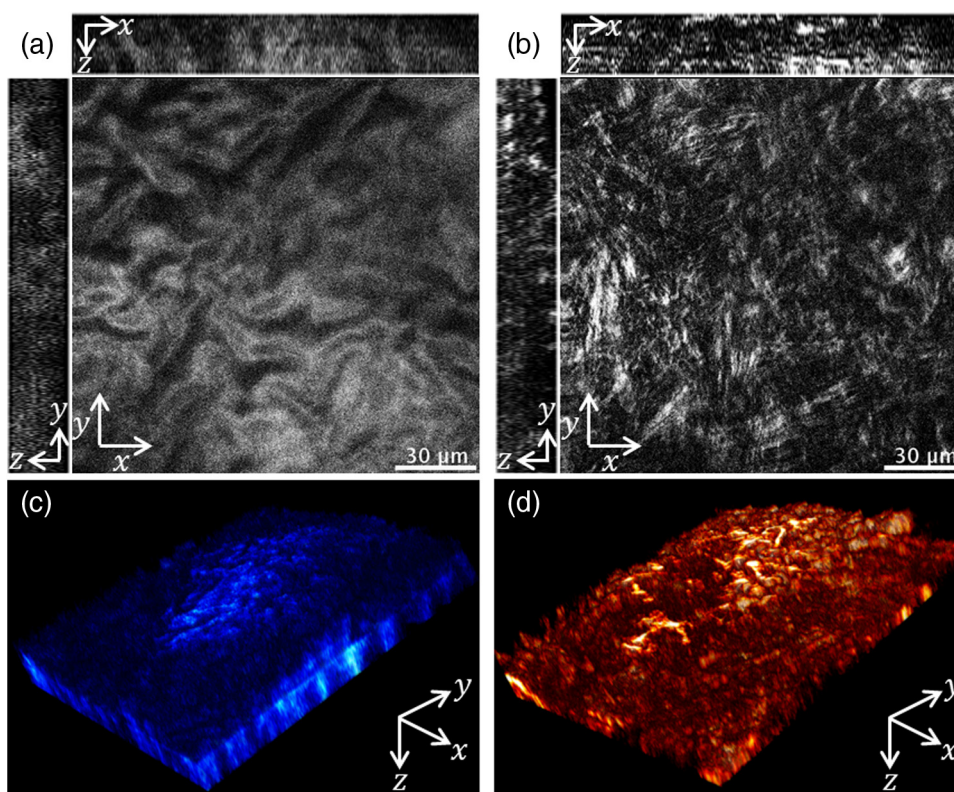
Morphological features such as layer thickness can also be measured using MPM. Here, the cornea epithelium, Descemet's membrane, and endothelium thicknesses were measured with a 2- μm error. The measured thicknesses are consistent with the ones reported in the literature.⁵

The autofluorescence lifetimes of NAD(P)H and flavins change upon protein-binding (essential to energy production). Thus, the assessment of free and protein-bound lifetime components, as well as their relative contributions, and free to protein-bound ratios enables one to infer about the cells metabolic state.

In the epithelial and endothelial layers, two autofluorescence lifetime components were observed for NAD(P)H (Table 1); a short lifetime associated with the free component of this fluorophore, and a long lifetime associated with the protein-bound component.^{41,42} Similar mean autofluorescence lifetimes were also reported for the porcine corneal epithelial layer.⁴³ Two autofluorescence lifetime components were also observed in the flavins range. The shorter lifetime is related to the protein-bound component; the longer to the unbound state. Shorter lifetimes were reported for FAD in the rat cornea and hamster cheek

Table 2 Porcine corneal epithelium free to protein-bound ratios for NAD(P)H and flavins at multiple depths. Values are represented as mean \pm standard deviation.

Corneal epithelial depth (μm)	free/(protein – bound) NAD(P)H	NAD(P)H normalized photon counts	free/(protein – bound) flavins	Flavins normalized photon counts
5	1.17 ± 0.31	1.00 ± 0.46	0.67 ± 0.24	0.54 ± 0.28
15	1.24 ± 0.30	0.91 ± 0.41	0.65 ± 0.21	0.49 ± 0.30
25	1.24 ± 0.35	0.90 ± 0.36	0.62 ± 0.22	0.49 ± 0.25
35	1.34 ± 0.34	0.87 ± 0.34	0.61 ± 0.20	0.47 ± 0.22
45	1.35 ± 0.37	0.86 ± 0.34	0.57 ± 0.18	0.46 ± 0.22
55	1.32 ± 0.29	0.85 ± 0.32	0.57 ± 0.22	0.45 ± 0.20
65	1.46 ± 0.32	0.80 ± 0.32	0.56 ± 0.21	0.43 ± 0.21
75	1.77 ± 0.42	0.70 ± 0.26	0.52 ± 0.24	0.44 ± 0.22


Fig. 6 Porcine corneal stroma SHG images and xz/yz projections in (a) backward and (b) forward direction, as well as (c) backward and (d) forward 3-D representations of approximately $153 \times 153 \times 40 \mu\text{m}^3$ reconstructed from individual and sequential SHG images with a $2\text{-}\mu\text{m}$ interval.

pouch epithelial cells.^{44,45} However, the fluorescence decay times of flavins bound to proteins are complex, and can vary between 0.1 to 5 ns.⁴¹ Furthermore, due to the overlap of NAD(P)H and flavins emission spectra,²⁵ NAD(P)H autofluorescence may still be detected in the flavins range (range II) which could influence the lifetimes and relative contributions.

Slight differences between the epithelium and endothelium NAD(P)H and flavins autofluorescence lifetimes were observed. This may indicate differences in the cell's metabolic activities. In particular, endothelial cells had a lower NAD(P)H free to

protein-bound ratio, suggesting a higher metabolic activity of this layer compared with the epithelium. These results are in accordance with the high metabolic activity of the corneal endothelial cells.^{3,46} However, in the flavins range, the opposite is observed. We believe that the low number of photons detected for this fluorophore [Fig. 2(a)] is insufficient for a reliable autofluorescence lifetime analysis.^{30,47}

A detailed analysis of the epithelial layer metabolic state was also performed. The NAD(P)H mean autofluorescence lifetime was decreased with depth (Fig. 5) and its free to protein-bound

ratio was increased (Table 2). This may suggest that the metabolic activity of epithelial cells decreases towards the inner part of the cornea, i.e., the metabolic activity is lowest for basal cells and highest for superficial cells. The obtained FLIM results are in agreement with the changes observed during stem cell differentiation. It has been demonstrated that fully differentiated cells have higher NAD(P)H mean autofluorescence lifetime and lower free to protein-bound ratios.^{48,49} Therefore, we speculate that the observed lifetime variations could be related to the differentiation properties of basal cells into wing and superficial cells. However, further studies are required to better understand this subject. To the best of our knowledge, the individual analysis of the metabolic activity of superficial, wing and basal cells based on FLIM was first described here.

In the stroma, two lifetime components were observed, reflecting the mixed autofluorescent compounds of collagen fibrils and keratocytes (Table 1). An individual analysis of both constituents was performed through the selection of regions of interest. Keratocytes had a shorter mean lifetime and higher free to protein-bound ratio than both the epithelial and endothelial cells. These results are most likely in accordance with the low metabolic activity of keratocytes, which are usually in a quiescent state.^{3,4}

The structural architecture of the corneal stroma was analyzed in both forward and backward directions using SHG. This imaging modality has already been demonstrated to be able to evaluate the structural organization of the porcine cornea stroma.^{50,51} As seen in Fig. 6, forward and backward detected SHG produce fairly distinct images [Figs. 6(a) and 6(b)]. The discrepancy between the forward and backward detected signals is correlated with the inability to resolve individual collagen fibrils due to their small diameters (25 to 35 nm). Due to the characteristics of backward detected SHG images, a straightforward determination of the collagen fibril orientation is difficult. However, since this detection configuration is the only one possible for an *in vivo* approach, efforts have been carried out to extract the stromal architecture.^{51,52}

The size and organization of fibrils varies with corneal depth. They become smaller and their arrangement more regular.³ In *xy/xz* projections and 3-D representations of the SHG signals (Fig. 6) a visualization of the corneal collagen architecture with depth was achieved.

Although mainly composed of collagen molecules,³ in the Descemet's membrane a strong autofluorescence signal was observed but no SHG photons were detected. This characteristic of the porcine Descemet's membrane has been previously described.⁵³ The generation of SHG from collagen is related not only to its microstructure but also to its macroscopic fibrillary structure.^{54,55} As such, the randomly organized collagen molecules in the Descemet's membrane do not produce SHG signals^{53,56} [Fig. 3(b)]. Two autofluorescence lifetime components were measured in this corneal layer, most likely correlated with collagen types IV and VII which compose this layer.⁴ However, further studies are required to understand Descemet's membrane autofluorescence. To the best of our knowledge, the autofluorescence lifetime of this corneal layer has not been described elsewhere.

5 Conclusion

In this study, we demonstrated the potential of MPM in the ophthalmological field through the characterization of the

porcine corneal layers with submicron spatial resolution, spectral resolution, and picosecond temporal resolution (5-D).

Using the autofluorescence intensity of the metabolic cofactors NAD(P)H and flavins the corneal cell morphology was determined. Spectral separation of signals from both metabolic cofactors was possible using a 16 channel PMT. However, due to the low sensitivity of the used PMT, higher exposure times were required to collect sufficient photon for fluorescence lifetime analysis when compared with a single channel PMT detector. Therefore, the 16 channel PMT is more suitable for fluorescence imaging of exogenous fluorophores, where the fluorescence intensity is normally higher than of endogenous fluorophores. Nevertheless, in this study we were able to retrieve information on the corneal cells metabolic states using the autofluorescence lifetime of the metabolic co-factors while keeping the radiation exposure below the damaging threshold. The analysis of the collagen fibrils architecture in 3-D was possible by SHG imaging.

In the future, we will assess the feasibility of the 5-D 12-fs laser microscope to characterize the human cornea. The evaluation of the cornea based on FLIM and SHG may give rise to new diagnostic methods, capable of early disease detection.

Acknowledgments

The authors would like to acknowledge the support by the Fundação para a Ciência e Tecnologia (FCT) projects PTDC/SAU-ENB/122128/2010 and PEST-C/SAU/UI3282/2013 and COMPETE programs FCOMP-01-0124-FEDER-021163 and FCOMP-01-0124-FEDER-037299. We thank JenLab GmbH for providing the required equipment and Miss Andrea Kaiser for the transport of the porcine eyes.

References

1. W. R. Zipfel, R. M. Williams, and W. W. Webb, "Nonlinear magic: multiphoton microscopy in the biosciences," *Nat. Biotechnol.* **21**(11), 1369–1377 (2003).
2. A. Periasamy and R. M. Clegg, *FLIM Microscopy in Biology and Medicine*, CRC Press, Boca Raton, Florida (2009).
3. L. A. Remington, *Clinical Anatomy of the Visual System*, 2nd ed., Elsevier, St. Louis, Missouri (2005).
4. J. H. Krachmer, M. J. Mannis, and E. J. Holland, *Cornea*, 3rd ed., Mosby/Elsevier, St. Louis, Missouri (2011).
5. I. Sanchez et al., "The parameters of the porcine eyeball," *Graefes Arch. Clin. Exp. Ophthalmol.* **249**(4), 475–482 (2011).
6. R. F. Steinert and D. Huang, *Anterior Segment Optical Coherence Tomography*, SLACK Incorporated, Thorofare, New Jersey (2008).
7. J. Kim et al., "Functional optical coherence tomography: principles and progress," *Phys. Med. Biol.* **60**(10), R211–R237 (2015).
8. T. Hillenaar, *In Vivo Confocal Microscopy Expanding Horizons in Corneal Imaging*, Erasmus University Rotterdam (2012).
9. P. Steven et al., "Comparison of Cornea Module and DermaInspect for noninvasive imaging of ocular surface pathologies," *J. Biomed. Opt.* **14**(6), 064040 (2009).
10. D. W. Piston, B. R. Masters, and W. W. Webb, "Three-dimensionally resolved NAD(P)H cellular metabolic redox imaging of the in situ cornea with two-photon excitation laser scanning microscopy," *J. Microsc.* **178**(Pt 1), 20–27 (1995).
11. B. Wang et al., "In-vivo corneal nonlinear optical tomography based on second harmonic and multiphoton autofluorescence imaging induced by near-infrared femtosecond lasers with rabbits," *Proc. SPIE* **5964**, 59640O (2005).
12. G. Karp, "Aerobic respiration and mitochondrion," in *Cell and Molecular Biology: Concepts and Experiments*, 6th ed., G. Karp, Ed., pp. 173–205, John Wiley & Sons, Hoboken, New Jersey (2009).

13. I. Bugiel, K. König, and H. Wabnitz, "Investigation of cells by fluorescence laser scanning microscopy with subnanosecond time resolution," *Laser Life Sci.* **3**(1), 47–53 (1989).
14. K. König, H. Schneckenburger, and R. Hibst, "Time-gated in vivo autofluorescence imaging of dental caries," *Cell Mol. Biol.* **45**(2), 233–239 (1999).
15. B. R. Masters, P. So, and E. Gratton, "Multi-photon excitation microscopy and confocal microscopy of human skin in vivo," *Comments Mol. Cell. Biophys.* **9**, 379–405 (1999).
16. K. König et al., "Optical tomography of human skin with subcellular spatial and picosecond time resolution using intense near infrared femtosecond laser pulses," *Proc. SPIE* **4620**, 191–201 (2002).
17. D. Schweitzer et al., "Time-resolved measurement autofluorescence. A method to detect metabolic changes in the fundus," *Ophthalmologie* **99**(10), 774–779 (2002).
18. D. Schweitzer et al., "Comparison of parameters of time-resolved autofluorescence between healthy subjects and patients suffering from early AMD," *Ophthalmologie* **106**(8), 714–722 (2009).
19. D. Schweitzer et al., "Fluorescence lifetime imaging ophthalmoscopy in type 2 diabetic patients who have no signs of diabetic retinopathy," *J. Biomed. Opt.* **20**(6), 061106 (2015).
20. S. Fine and W. P. Hansen, "Optical second harmonic generation in biological systems," *Appl. Opt.* **10**(10), 2350–2353 (1971).
21. L. Tian et al., "Microscopic second-harmonic generation emission direction in fibrillous collagen type I by quasi-phase-matching theory," *J. Appl. Phys.* **108**(5), 54701–54709 (2010).
22. N. Morishige et al., "Second-harmonic imaging microscopy of normal human and keratoconus cornea," *Invest Ophthalmol. Vis. Sci.* **48**(3), 1087–1094 (2007).
23. R. McQuaid et al., "Second-harmonic reflection imaging of normal and accelerated corneal crosslinking using porcine corneas and the role of intraocular pressure," *Cornea* **33**(2), 125–130 (2014).
24. Z. Földes-Papp et al., "Trafficking of mature miRNA-122 into the nucleus of live liver cells," *Curr. Pharm. Biotechnol.* **10**(6), 569–578 (2009).
25. A. Batista et al., "Characterization of porcine eyes based on autofluorescence lifetime imaging," *Proc. SPIE* **9329**, 93290E (2015).
26. T. Ehmke et al., "Spectral behavior of second harmonic signals from organic and non-organic materials in multiphoton microscopy," *AIP Adv.* **5**(8), 084903 (2015).
27. P. J. Campagnola et al., "Three-dimensional high-resolution second-harmonic generation imaging of endogenous structural proteins in biological tissues," *Biophys. J.* **82**(1), 493–508 (2002).
28. E. Birngruber, R. Donner, and G. Langs, "MatVTK—3D Visualization for Matlab," in *Proceedings of the MICCAI 2009 Workshop on systems and architectures for CAI*, pp. 1–8 (2009).
29. C. A. Poole, N. H. Brookes, and G. M. Clover, "Confocal imaging of the keratocyte network in porcine cornea using the fixable vital dye 5-chloromethylfluorescein diacetate," *Curr. Eye Res.* **15**, 165–174 (1996).
30. W. Becker et al., "Fluorescence lifetime imaging by time-correlated single-photon counting," *Microsc. Res. Tech.* **63**(1), 58–66 (2004).
31. K. König et al., "Optical skin biopsies by clinical CARS and multiphoton fluorescence/SHG tomography," *Laser Phys. Lett.* **8**(6), 465–468 (2011).
32. S. Huang, A. A. Heikal, and W. W. Webb, "Two-photon fluorescence spectroscopy and microscopy of NAD(P)H and flavoprotein," *Biophys. J.* **82**(5), 2811–2825 (2002).
33. B. R. Masters et al., "Pyridine nucleotides and phosphorylation potential of rabbit corneal epithelium and endothelium," *Invest Ophthalmol. Vis. Sci.* **30**(5), 861–868 (1989).
34. D. W. Batey and C. D. Eckhart, "Analysis of flavins in ocular tissues of the rabbit," *Invest Ophthalmol. Vis. Sci.* **32**(7), 1981–1985 (1991).
35. K. König and I. Riemann, "High-resolution multiphoton tomography of human skin with subcellular spatial resolution and picosecond time resolution," *J. Biomed. Opt.* **8**(3), 432–439 (2003).
36. S. W. Teng et al., "Multiphoton autofluorescence and second-harmonic generation imaging of the ex vivo porcine eye," *Invest Ophthalmol. Vis. Sci.* **47**(3), 1216–1224 (2006).
37. B. G. Wang et al., "High-resolution two-photon excitation microscopy of ocular tissues in porcine eye," *Lasers Surg. Med.* **40**(4), 247–256 (2008).
38. K. König, O. Krauss, and I. Riemann, "Intracorneal surgery with 80 MHz nanosecond femtosecond laser pulses in the near infrared," *Opt. Express* **10**(3), 171–176 (2002).
39. W. T. Mason, *Fluorescent and Luminescent Probes for Biological Activity: A Practical Guide to Technology for Quantitative Real-Time Analysis*, 2nd ed., Elsevier Science, London, United Kingdom (1999).
40. S. E. Lee et al., "Characterization of porcine corneal endothelium for xenotransplantation," *Semin. Ophthalmol.* **29**, 1–9 (2013).
41. J. R. Lakowicz, *Principles of Fluorescence Spectroscopy*, 3rd ed., Springer, New York (2007).
42. J. R. Lakowicz et al., "Fluorescence lifetime imaging of free and protein-bound NADH," *Proc. Natl. Acad. Sci. U. S. A.* **89**(4), 1271–1275 (1992).
43. K. König et al., "Applications of multiphoton tomographs and femtosecond laser nanoprocessing microscopes in drug delivery research," *Adv. Drug Delivery Rev.* **63**(4–5), 388–404 (2011).
44. A. Batista et al., "Fluorescence Lifetime based Corneal Metabolic Imaging," *Procedia Technol.* **17**, 281–288 (2014).
45. M. C. Skala et al., "In vivo multiphoton microscopy of NADH and FAD redox states, fluorescence lifetimes, and cellular morphology in precancerous epithelia," *Proc. Natl. Acad. Sci. U. S. A.* **104**(49), 19494–19499 (2007).
46. L. Bye, N. Modi, and M. Stanford, *Basic Sciences for Ophthalmology*, Oxford University Press, Oxford, United Kingdom (2013).
47. W. Becker, *Advanced Time-Correlated Single Photon Counting Applications*, Springer International Publishing, Switzerland (2015).
48. K. König, A. Uchugonova, and E. Gorjup, "Multiphoton fluorescence lifetime imaging of 3D-stem cell spheroids during differentiation," *Microsc. Res. Tech.* **74**(1), 9–17 (2011).
49. C. Stringari et al., "Metabolic trajectory of cellular differentiation in small intestine by Phasor Fluorescence Lifetime Microscopy of NADH," *Sci. Rep.* **2**, 568 (2012).
50. B. Vohnsen and P. Artal, "Second-harmonic microscopy of ex vivo porcine corneas," *J. Microsc.* **232**(1), 158–163 (2008).
51. G. Latour et al., "In vivo structural imaging of the cornea by polarization-resolved second harmonic microscopy," *Biomed. Opt. Express* **3**(1), 1–15 (2012).
52. H. G. Breunig et al., "Motionless polarization-resolved second harmonic generation imaging of corneal collagen," *Proc. SPIE* **9329**, 93292P (2015).
53. L. Jay et al., "Determination of porcine corneal layers with high spatial resolution by simultaneous second and third harmonic generation microscopy," *Opt. Express* **16**(21), 16284 (2008).
54. T. A. Theodossiou et al., "Second harmonic generation confocal microscopy of collagen type I from rat tendon cryosections," *Biophys. J.* **91**(12), 4665–4677 (2006).
55. A. T. Yeh et al., "Reversible dissociation of collagen in tissues," *J. Invest Dermatol.* **121**(6), 1332–1335 (2003).
56. F. Aptel et al., "Multimodal nonlinear imaging of the human cornea," *Invest Ophthalmol. Vis. Sci.* **51**(5), 2459–2465 (2010).

Ana Batista obtained her master's degree in biomedical engineering in 2010 at the Faculty of Sciences and Technology of the University of Coimbra. In September 2013, she enrolled the biomedical engineering PhD program of the Faculty of Sciences and Technology of the University of Coimbra. Her current research activities aim to study the morphology and metabolism of corneal tissues using multiphoton microscopy techniques, such as two-photon excitation fluorescence lifetime imaging microscopy, and second- and third-harmonic generation.

Hans Georg Breunig has worked for more than ten years on applications of femtosecond-laser pulses in different research fields. He holds a master's degree in physics from the University of Maryland at College Park, USA, and received a PhD in physics for experimental studies on ultrafast excitations in quantum structures from the University of Bremen, Germany. Afterwards, he concentrated on the control of competing chemical processes with ultrashort pulses at the Philipps-University Marburg, Germany. Hans Georg Breunig is the author of more than 30 journal papers and now a research scientist at JenLab GmbH.

Aisada Uchugonova received her master's degree in biomedical sciences from the National University of Kyrgyzstan in 2003 and her PhD degree from the Saarland University, Faculty of Medicine in Homburg, Germany. She served as a postdoctoral researcher at Anticancer Inc. and at the University of California San Diego. She is currently PI on the DFG-funded project in the Department of Biophotonics and Laser Technology, Saarland University. Her research interests include non-invasive and label-free imaging, optical characterization of stem cells, and nanosurgery of cells.

António Miguel Morgado received his PhD degree in physics and is assistant professor in the Department of Physics of the University of Coimbra. He is a researcher at the Institute for Biomedical Imaging and Life Sciences, where he works mainly on the development of optoelectronic instrumentation and techniques for ocular imaging, namely corneal metabolic imaging using fluorescence lifetime

microscopy, corneal confocal microscopy and retinal OCT imaging. His research interests also include low-level laser therapy and laser safety.

Karsten König studied physics in Rostock, wrote his PhD and habilitation thesis in Jena, and worked at the Institute for Laser Technologies in Ulm, at the Beckman Laser Institute in Irvine, at the Institute for Molecular Biotechnology in Jena and at the University Jena. He is currently full professor for biophotonics and laser technology at the Faculty of Physics and Mechatronics at Saarland University in Saarbrücken, Germany. He is co-founder of the spin-off company JenLab GmbH. He is author of more than 200 publications and received a variety of awards such as the Fraunhofer Award Technik für den Menschen, the Kortum Motivationspreis, the Pascal Rol Award of the SPIE, the Feulgen Prize, and the Award for Applied Research of the State of Thuringia.